This is a repository copy of *Near-UV photodissociation dynamics of CH2I2*.

White Rose Research Online URL for this paper:
http://eprints.whiterose.ac.uk/97214/

Version: Accepted Version

Article:

Near-UV photodissociation dynamics of CH$_2$I$_2$

Benjamin W. Toulson, Jonathan P. Alaniz, and Craig Murray[1]

Department of Chemistry, University of California, Irvine, Irvine CA 92697, USA

J. Grant Hill[2]

Department of Chemistry, University of Sheffield, Sheffield S3 7HF, UK

---

[1] Email: craig.murray@uci.edu; Telephone: +1-949-824-4218
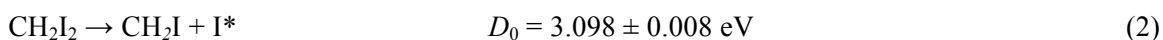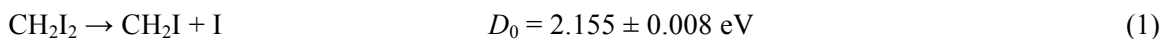
[2] Email: grant.hill@sheffield.ac.uk; Telephone: +44-(0)114-222-9392

Abstract

The near-UV photodissociation dynamics of CH_2I_2 has been investigated using a combination of velocity-map (slice) ion imaging and *ab initio* calculations characterizing the excited states. Ground state $I(^2P_{3/2})$ and spin-orbit excited $I^*(^2P_{1/2})$ atoms were probed using 2+1 resonance-enhanced multiphoton ionization (REMPI) or with single-photon VUV ionization. Two-color ion images were recorded at pump wavelengths of 355 nm, 266 nm and 248 nm, and one-color ion images at the REMPI wavelengths of ~304 nm and ~280 nm. Analysis of the ion images shows that, regardless of iodine spin-orbit state, ~20% of the available energy is partitioned into translation E_T at all excitation wavelengths indicating that the CH_2I co-fragment is formed highly internally excited. The translational energy distributions comprise a slow, "statistical" component that peaks near zero and faster components that peak away from zero. The slow component makes an increasingly large contribution to the distribution as the excitation wavelength is decreased. The C–I bond dissociation energy of $D_0 = 2.155 \pm 0.008$ eV is obtained from the trend in the E_T release of the faster components with increasing excitation energy. The I and I* ion images are anisotropic, indicating prompt dissociation, and are characterized by β parameters that become increasingly positive with increasing E_T. The decrease in β at lower translational energies can be attributed to deviation from axial recoil. MRCI calculations including spin-orbit coupling have been performed to identify the overlapping features in the absorption spectrum and characterize one-dimensional cuts through the electronically excited potential energy surfaces. The excited states are of significantly mixed singlet and triplet character. At longer wavelengths, excitation directly accesses repulsive states primarily of B_1 symmetry, consistent with the observed $\langle \beta \rangle$, while shorter wavelengths accesses bound states, also of B_1 symmetry that are crossed by repulsive states.

Introduction

Diiodomethane (CH_2I_2) is one of the most important sources of iodine atoms in the marine boundary layer.[1,2] Tropospheric iodine chemistry exerts an influence on the oxidative capacity of the atmosphere and can also lead to new particle formation.[2] The reaction of iodine atoms with ozone forms iodine monoxide (IO), which can subsequently react with HO_2 or NO_2 to form photolabile products that may participate in catalytic ozone destruction[2,3] and accounts for ~50% of the total ozone loss in the MBL.[4] The chemistry is initiated by photolysis. CH_2I_2 absorbs strongly at $\lambda < 360$ nm[5,6] overlapping significantly with the solar spectrum and the large photolysis rate results in an atmospheric lifetime of only a few minutes.[6] The photolysis products are predominantly iodomethyl radicals and either ground $I(^2P_{3/2})$ or spin-orbit excited $I(^2P_{1/2})$ atoms (henceforth labelled I and I*, respectively), with a combined quantum yield, Φ, of unity.[7–9]

$$CH_2I_2 \rightarrow CH_2I + I \qquad\qquad D_0 = 2.155 \pm 0.008 \text{ eV} \qquad\qquad (1)$$

$$CH_2I_2 \rightarrow CH_2I + I^* \qquad\qquad D_0 = 3.098 \pm 0.008 \text{ eV} \qquad\qquad (2)$$

The bond dissociation energies have been derived from the results of this work (*vide infra*). An additional minor channel forming $CH_2 + I_2$ ($\Phi = 0.004$) has been identified at an excitation wavelength of 248 nm.[10] Recently, diiodoalkanes have been widely used as iodoalkyl radical precursors used for laboratory production of atmospherically important carbonyl oxide biradicals, or Criegee intermediates by reaction with molecular oxygen.[11,12] Recently, we have reported preliminary evidence suggesting that the degree of internal excitation in the photolytically-generated CH_2I radical may affect the kinetics and product branching of the $CH_2I + O_2$ reaction.[13] A major motivation for this work was characterization of the CH_2I internal energy distribution at common photolysis wavelengths, with a view to exploring its influence on kinetics.

The near-UV absorption spectrum of CH_2I_2 at 298 K, shown in Figure 1, has typically been deconvolved into four Gaussian components, but is otherwise unstructured.[14] Assignments have been derived from an

exciton model proposed by Kawasaki *et al.* that treats the molecule as a pair of weakly coupled chromophores. The model predicts six electronic states in C_{2v} symmetry, although transitions to the state of A_2 symmetry are electric dipole forbidden.[15] The intense long wavelength band is assigned to two overlapping bands centered at 312 and 286 nm, both of B_1 symmetry. The weaker feature at 250 nm is attributed to unresolved transitions to B_2 and A_1 states. A state of A_1 symmetry is responsible for the intense short wavelength absorption band at 214 nm. Subsequent magnetic circular dichroism (MCD) measurements, however, suggest that the first absorption band corresponds to excitation to states of B_1 and B_2 symmetry and identify the state responsible for the band at 248 nm as A_1.[16] The MCD measurements also reveal a weak shoulder near the long-wavelength onset of the first absorption band that was attributed to a nominally forbidden transition, most probably a triplet state.[16] Electronic structure calculations on CH_2I_2 are limited and the predicted electronic state symmetries disagree with the exciton model. Zheng and Phillips used time-dependent density functional theory (TD-DFT) to characterize the first five singlet (and triplet) excited electronic states, resulting in assignments that agree with the interpretation of the MCD experiments.[17] More recent calculations have characterized the electronic states using the CASPT2 method[18] and TD-DFT,[19] although only the former study included spin-orbit coupling. Unsurprisingly for a molecule with two iodine atoms many of the excited states have strongly mixed singlet and triplet character. An apparent discrepancy between the CASPT2 and earlier TD-DFT results in the identification of the excited valence states can be attributed to the choice of coordinate system, which switches the B_1 and B_2 labels. Here we adopt the convention established first, in which the C_2 symmetry axis is defined as the *z*-axis and the *y*-axis is normal to the heavy atom plane.

Several groups have investigated the photodissociation dynamics of CH_2I_2 in the gas phase and the band assignments derived from the exciton model have formed the basis of almost all interpretation of the experimental data. Photofragment translational spectroscopy (PTS) experiments with mass spectrometric detection of photoproducts were performed by Kawasaki *et al.* using broadband excitation centered at 310 nm, and spanning the first absorption band. Analysis of the angular distribution of the

photofragments resulted in an anisotropy parameter of $\beta = 0.9$, indicative of prompt dissociation after excitation to states of B_1 symmetry, consistent with the results of their exciton model. Similar experiments at a shorter photolysis wavelength of 266 nm measured angular distributions in excellent accord with Kawasaki *et al.*, and also photofragment flight times that indicated the production of highly-internally excited CH_2I.[20] Baughcum and Leone observed strong infrared emission across the range 590–4100 cm^{-1} after photolysis at 308 and 248 nm, concluding that CH_2I radicals are produced with internal excitation corresponding to a quasi-continuum density of states. Strong distinct emission features were observed in the CH stretch (up to four quanta), CH_2 bending and combination regions.[7]

The branching between I and I* depends strongly upon the excitation wavelength. The quantum yield for I* over the wavelength range 248–366 nm has been independently measured by atomic emission spectroscopy.[7,8] and photoacoustic yield spectroscopy.[9] While the latter technique resulted in slightly smaller I* yields, both measurements agree that the quantum yield for I* is effectively zero at 355 nm and monotonically increases towards shorter wavelength, approaching $\Phi = 0.5$ at 248 nm. When scaled by the absorption cross section, the I* yield apparently maps the second Gaussian component representing excitation to the second electronic state, as shown in Figure 1, suggesting that this state correlates with spin-orbit excited I* atoms. The observation that I atoms are also formed was attributed to a curve crossing mechanism.[9]

2+1 REMPI spectroscopy has also been used to detect I and I* photoproducts, exploiting probe transitions with wavelengths falling within the first absorption band of CH_2I_2. Jung *et al.* used time-of-flight mass spectrometry to measure product velocity distributions, dissociating CH_2I_2 and probing I and I* near 304 nm. I* atoms were found to be the minor product, with $\Phi = 0.25$, the low recoil velocities confirmed extensive internal excitation of the CH_2I radical fragment. The anisotropy parameters of 0.4 and 0.55 for formation of I and I* atoms, respectively, are generally smaller than the earlier PTS experiments, and the limiting value, but still consistent with a transition to a dissociative B_1 state.[21] A similar one-color dissociation and ionization approach was taken by Xu *et al.* who used several wavelengths between 277

and 304 nm with velocity-map imaging (VMI) detection of I and I*.[22] The total translational energy

distributions obtained probing I atoms were deconvolved into two major Gaussian components, each of

which showed a positive β. In contrast, translational energy distributions obtained after imaging I* were

dominated by a single component that shared the value β of the slower I atom component. Following the

exciton model state assignments, the 1^1B_1 state correlates with $CH_2I + I$ and produces I atoms exclusively.

The higher-lying 2^1B_1 state correlates adiabatically with $CH_2I + I*$ atoms, but may also produce I atoms

by non-adiabatic coupling to the lower 2^1A_1 state. More recently, Lehman *et al.* used two-color VMI

experiments to examine the photochemistry of CH_2I_2 at 248 nm, using 2+1 REMPI at 313 nm to probe I*

atoms.[23] The probe wavelength is strongly absorbed by the parent molecule and resulted in intense one-

color signals. After subtraction, the translational energy distributions were again consistent with highly

internally excited CH_2I fragments but showed some evidence of bimodality. The measured $\beta = 0.81\pm0.05$

is consistent with prompt dissociation after a transition to a B_1 state, and is not in accord with either the

exciton model or the MCD assignment.[23] Some consistent trends in the photodissociation dynamics

emerge over the photolysis wavelength range 248–310 nm. The average fraction of the available energy

partitioned into the internal modes of the CH_2I radical is consistently $f_{INT} \approx 0.8$–0.9, regardless of the

iodine atom spin-orbit level. The dissociation appears to be prompt and the angular anisotropy at all

excitation wavelengths suggests parallel transitions, predominantly to states of B_1 symmetry. Neither the

initially excited electronic state nor changes in total energy available appear to significantly change the

photodissociation dynamics. The characters of the electronically excited states, however, remain the

subject of some uncertainty.

In this paper we report new experimental measurements that systematically examine the photodissociation

dynamics of CH_2I_2 following excitation at five wavelengths spanning the near-UV absorption spectrum.

DC slice velocity-map imaging (VMI) has been combined with state-selective resonance-enhanced

multiphoton ionization (REMPI) or vacuum ultraviolet ionization (VUV) to probe I and I* atoms. The

experimental measurements are complemented by electronic structure calculations, including the effects

of spin-orbit coupling, which characterize the electronically excited states responsible for the absorption spectrum and the photochemistry.

Experiment

Experiments were performed in a recently constructed DC slice velocity-map imaging (VMI) spectrometer. The apparatus consists of source, ionization and drift/detection regions, each evacuated by dedicated turbomolecular pumps (Leybold 1100C, Pfeiffer 700M and Leybold 360) backed by an oil-free Roots pumps (Adixen one ACP28G, and two ACP15G) to base pressures of $\sim4\times10^{-7}$ Torr.

A liquid sample of CH_2I_2 (Sigma-Aldrich, 99% purity) was stored in a stainless-steel bubbler. Ar carrier gas at a pressure of ~1 atm passed over the sample and was supersonically expanded into the source region using a solenoid pulsed valve (General Valve Series 9). The expansion was skimmed (Beam Dynamics Inc.) between the source and ionization regions to form a molecular beam, directed along the time-of-flight axis. Based on the vapor pressure of CH_2I_2 at 295 K, we estimate that the molecular beam comprised ~0.15% CH_2I_2. The pressure in the source region increased to 2×10^{-6} Torr during valve operation.

The CH_2I_2/Ar molecular beam was intersected by counter-propagating pump (photolysis) and probe laser beams, λ_{pump} and λ_{probe} in the center of a stack of velocity-mapping electrodes, optimized for DC slicing of the ion cloud. The pump beam spans the range 248–355 nm and is generated using a tunable mid-band optical parametric oscillator (OPO) pumped by the third harmonic of a Nd:YAG laser (Continuum Horizon II and Surelite EX). The pump beam was focused using a fused silica lens (f = 300 mm). Pulse energies were typically < 1 mJ, which coupled with the relatively broad OPO bandwidth of ~5 cm^{-1} give a low peak intensity and reduces the likelihood of driving (resonant) multiphoton dissociation processes. Iodine atoms formed in the dissociation were probed approximately 10–20 ns after photolysis using both single-photon VUV ionization and 2+1 REMPI. The VUV beam at λ_{probe} = 118.2 nm was generated by frequency tripling the third harmonic of a Nd:YAG laser (Continuum Surelite II-10) in a low pressure

7

static gas cell containing a phase-matched mixture of Xe and Ar (1:50 ratio at P < 50 Torr). The

attenuated 355 nm beam (< 8 mJ) was gently focused into the cell by an external fused silica lens (f = 500

mm) while an internal MgF_2 lens (f = 200 mm), which also acts as a window to separate the mixing cell

from the high-vacuum ionization region, focused the VUV into the molecular beam and approximately re-

collimates the residual 355 nm. Optimization of phase-matching was achieved while monitoring VUV

ionization of the CH_2I_2 parent molecule. The REMPI probe beam was generated by frequency doubling

in β-barium borate (BBO) the fundamental output of a Nd:YAG-pumped dye laser (Lambda-Physik

Scanmate 2 and Continuum Surelite II-10) operating with either Rhodamine 590 or 640 dyes.

The laser sources generate horizontally polarized radiation, while the experiment requires both pump and

probe pulses to be vertically polarized. The polarization of the pump radiation from the OPO was rotated

using a combination of a variable phase retardation wave plate (Alphalas GmbH) set to act as a half-wave

plate and a Rochon polarizer (MgF_2, Edmund Optics). The fixed-frequency VUV polarization was

controlled by placing a 355 nm half-wave plate in the beam path of the Nd:YAG third harmonic. The

REMPI probe polarization was rotated using a photo-elastic modulator (PEM) and delay pulse generator

(Hinds Instruments PEM-100 and DPG-5000), capable of performing arbitrary phase retardation of laser

pulses. The delay pulse generator synchronizes the intrinsic 50 kHz oscillation frequency of the PEM

crystal with the 10 Hz repetition rates of other components, by externally triggering an eight-channel

digital delay generator (Quantum Composers 9528) at 10 Hz, which in turn controls the synchronization

of all other components.

The velocity-mapping ion optics stack comprises five electrodes optimized for DC slicing[24] of the

expanded ion cloud and the construction follows an established design.[25] Velocity-mapping is obtained

with an extractor-to-repeller voltage ratio of 0.87. The detector comprises a pair of 40 mm diameter

chevron-stacked microchannel plates (MCPs) coupled to a P46 phosphor screen (Photonis). A fast high

voltage switch (Photek GM-MCP-2) was used to pulse the voltage applied to the rear MCP, which limited

the effective gain to only 22 ns. The arrival time of the I^+ ions was stretched to 135 ns, hence only 16%

of the full ion packet is detected, satisfying the requirements for a narrow central slice.[24]

Images were acquired at the 10 Hz repetition rate of the lasers using a CCD camera (Basler a312f, 782×

582 pixels) and transferred to the data acquisition (DAQ) PC for pre-processing in real time. Event

counting was performed in software, using both spot size and intensity to discriminate between genuine

ion strikes and background counts. Sub-pixel precision was achieved by calculating the centroid of each

ion strike and is used to upscale a native 512×512 pixel region of interest chosen, by a factor of two to

1024×1024. During image acquisition, the total phosphorescence emitted by the detector screen, and the

pump and probe laser pulse energies are monitored by a silicon photomultiplier (SenSL, MicroSL 10020-

X18) and a photodiode (Thorlabs, DET-10A), respectively. These signals are acquired by an oscilloscope

(Teledyne Lecroy, HDO4054), which is also interfaced to the DAQ PC.

Automated routines are implemented in the data acquisition software (National Instruments, Labview

2013) to maximize the robustness of data acquisition and minimize the impact of long-term variations in

experimental conditions. Images are acquired in sets, each of which involves cycling (typically for 2500

shots) over several different pump wavelengths while the probe laser is repeatedly scanned across the

Doppler profile. In addition to two-color [pump + probe] images, [pump only] and [probe only] images

were also acquired to allow removal of one-color background signals. The process was repeated until the

desired signal-to-noise ratio was achieved. Individual measurement sets (~300,000 laser shots/image)

were repeated three times. Where appropriate, the one-color background signals were subtracted prior to

any further image analysis.

Spectrometer Calibration

Photofragment speeds, v, are related to the image radius, R (in pixels), by

$$v = NR/t \tag{3}$$

where N is a calibration factor that must be determined empirically, and t is the flight time of the detected photofragment. The well-studied photodissociation of OCS was used to provide images to calibrate the VMI spectrometer:[26]

$$OCS \rightarrow CO + S(^1D) \qquad\qquad D_0 = 4.2908 \pm 0.0030 \text{ eV} \qquad\qquad (4)$$
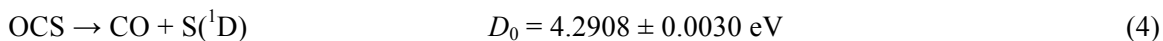
Excitation in the wavelength range 222–250 nm leads to prompt dissociation, forming predominantly CO $X^1\Sigma^+(v = 0, J)$ and $S(^1D)$, which was probed using 2+1 REMPI via the $^1F_3$ state at a one-photon probe wavelength of 288.18 nm. The calibration set is based on the photodissociation of OCS at λ_{pump} = 222, 235 and 250 nm. The calibration factor was adjusted to best match the resolved high-J levels of the CO(v=0) fragment to a rotational comb calculated using previously reported spectroscopic constants for CO.[27] The accuracy of the scaling factor was cross-checked using published data from several previous studies of OCS photodissociation.[26,28–30]

Theory

The electronic ground state geometry of CH$_2$I$_2$ was optimized at the explicitly correlated coupled cluster with single, double and perturbative triple excitations [CCSD(T)-F12b] level of theory,[31,32] using the correlation consistent cc-pVQZ-F12 basis sets for carbon and hydrogen,[33] and the cc-pVQZ-PP-F12 basis set paired with the small-core relativistic pseudopotential (PP) ECP28MDF for iodine.[34,35] The density fitting of the Fock and exchange matrices used the cc-pVQZ/JKFit and def2-QZVPP/JKFit auxiliary basis sets,[36,37] while the aug-cc-pwCV5Z/MP2Fit and cc-pVQZ-PP-F12/MP2Fit sets were used in the density fitting of the remaining two-electron integrals.[34,38] The many-electron integrals arising in explicit correlation theory were accurately and efficiently approximated using the resolution-of-the-identity method with cc-pVQZ-F12/OptRI and cc-pVQZ-PP-F12/OptRI used in the complementary auxiliary basis set (CABS) approach.[34,39,40] The geminal Slater exponent was set to 1.0 a$_0^{-1}$ in all cases. Such combinations of basis sets and pseudopotentials will be referred to as cc-pVnZ-F12 herein. Initial testing demonstrated that CCSD(T)-F12b/cc-pVDZ-F12 produced an almost identical geometry as explicitly

correlated internal contracted multi-reference configuration interaction with the Davidson correction (MRCI-F12+Q),[41–43] hence the more computationally tractable coupled cluster method was used for geometry optimization with larger basis sets. The vertical excitations energies of the first 19 excited states ($3 \times {}^1A_1$, $2 \times {}^1B_1$, $2 \times {}^1B_2$, $2 \times {}^1A_2$, $3 \times {}^3A_1$, $3 \times {}^3B_1$, $2 \times {}^3B_2$, and $2 \times {}^3A_2$) were obtained at the MRCI-F12+Q/cc-pVQZ-F12 level based on a full-valence complete-active-space self-consistent field (CASSCF) reference. The CABS singles correction was applied to the CASSCF reference energies.[44] In order to calibrate the error in the MRCI-F12+Q vertical excitation energies, the adiabatic excitation energy to the first triplet excited state was compared to that obtained from the composite coupled cluster approach of Peterson *et al.*[45] This protocol includes corrections for basis set incompleteness, core-valence effects, scalar relativity and higher order correlation, thus it should provide almost exact Born-Oppenheimer approximation results in the absence of spin-orbit coupling. The MRCI-F12+Q results were found to overestimate the excitation energy by 0.09 eV, indicating that resulting calculated absorption spectra may be slightly blue-shifted relative to experiment. Spin-orbit coupling was conducted on the 19 spin-free states at the MRCI level using the cc-pVQZ-PP basis and PP for iodine and the cc-pVQZ basis for all other elements.[35,46] For iodine the spin-orbit operator defined in the pseudopotential was used, while the Breit-Pauli operator was used for lighter atoms. The energy eigenvalues computed in the preceding MRCI/cc-pVQZ calculation were replaced by those precomputed at the MRCI-F12+Q/cc-pVQZ-F12 level, hence only the spin-orbit matrix elements are computed at the lower level of theory.

Potential energy curves were computed by scanning along a single C–I bond distance and keeping all other internal coordinates fixed at the equilibrium geometry. The reduction in symmetry from C_{2v} to C_s necessitated that these calculations were carried out at the MRCI-F12+Q/cc-pVDZ-F12 level of theory, including the first 17 spin-free states ($5 \times {}^1A'$, $4 \times {}^1A''$, $4 \times {}^3A'$, and $4 \times {}^3A''$, these states were selected based on an inspection of the contributions of the spin-free states to the composition of the spin-orbit eigenvectors at the equilibrium geometry). This resulted in a total of 33 spin-orbit coupled levels calculated at the MRCI level with cc-pVDZ-PP for iodine and cc-pVDZ for all other elements. Again,

11

the energy eigenvalues of the spin-free states were replaced by those computed at the MRCI-F12+Q/cc-pVDZ-F12 level.

All calculations were performed using the MOLPRO 2012.1 quantum chemistry package.[47,48]

Results

DC sliced velocity-map ion images of I and I* atom products have been recorded following excitation of CH_2I_2 at pump wavelengths of 355 nm, 266 nm and 248 nm. Single photon VUV ionization was used to detect ground state I atoms, while 2+1 REMPI at one-photon wavelengths near 281 nm and 304 nm was used to detect both I and I*. Since CH_2I_2 absorbs strongly at the REMPI probe wavelengths, one-color probe only images provide data at these additional wavelengths. Extraction of the two-color signal, however, requires a careful background subtraction procedure when using the REMPI detection schemes. The energy available E_{AVL} to the photofragments after cleavage of a C–I bond is

$$E_{AVL} = h\nu - D_0 = E_{INT} - E_{SO} - E_T \tag{5}$$

where $h\nu$ is the pump photon energy and D_0 is the bond dissociation energy. E_{AVL} can be partitioned into internal excitation (rotation and vibration) of the CH_2I radical E_{INT}, spin-orbit excitation of the iodine atom E_{SO} (zero for I and 0.9426 eV for I*) and relative translation E_T, which is derived from the images. It is assumed that the CH_2I_2 parent has near-zero internal energy prior to absorption of the pump photon as a result of cooling in the supersonic expansion.

VUV ionization provides an effectively state selective means of detecting ground state I atoms. Iodine has an ionization potential of 10.45126 eV, which is marginally less than the 10.49 eV VUV photons generated by frequency tripling the Nd:YAG 3rd harmonic. At 118.2 nm, an accidental resonance with an autoionizing Rydberg state results in 19.2 times greater sensitivity for I over I*.[49,50] The I* quantum yield increases monotonically from zero at 355 nm to a maximum of around 0.46 at 248 nm. Consequently, I* atoms account for at most ~2% of the total ion counts in the images acquired using the VUV probe.[8] CH_2I can also be ionized at 118.2 nm, but the CH_2I^+ signal in the mass spectrum was around an order of

magnitude weaker than that of I$^+$ this product was not pursued for imaging studies. Ion images recorded using VUV detection of I atoms formed from the photodissociation of CH$_2$I$_2$ at 355 nm, 266 nm and 248 nm are shown in Figure 2. Relatively minor pump-only and probe-only contributions have been subtracted. At all pump wavelengths, the maximum observed I atom speed is significantly slower than the maximum possible. At 355 nm, the anisotropic ring shown in Figure 2 corresponds to formation of I atoms with speeds of ~450 m s^{-1}. The radius of the ring increases at 266 nm and 248 nm, indicating speeds of >600 m s^{-1}, and becomes more diffuse. A slower component in the center of the image is evident at 266 nm and increases in intensity at 248 nm.

2+1 REMPI was also used to probe atomic iodine products. Ground state I atoms were probed *via* the (^{3}P$_1$)6p[0]$_{1/2}$ and (^{3}P$_2$)6p[1]$_{1/2}$ states at λ$_{probe}$ = 279.71 nm and 303.69 nm. Spin-orbit excited I* atoms were probed *via* the (^{1}D$_2$)6p[3]$_{5/2}$ and (^{3}P$_1$)6p[1]$_{1/2}$ states at nearby λ$_{probe}$ = 281.73 nm and 304.03 nm.[21] Use of 2+1 REMPI to detect I and I* is complicated by strong absorption of the CH$_2$I$_2$ parent at the probe wavelengths, which are near the first absorption maximum (see Figure 1). Strong one-color, probe-only signals where λ$_{pump}$ = λ$_{probe}$ are unavoidable. Figure 3 shows typical one-color ion images probing I* atoms at both REMPI probe wavelengths alongside the equivalent two-color images recorded using a photolysis wavelength of 266 nm and the images resulting from a scaled subtraction procedure (described below). The one-color images [Figures 3(a) and 3(d)] are dominated by an intense outermost ring, and a slower component that makes a relatively larger contribution at 282 nm. The radii of the outer rings depend upon photolysis wavelength and correspond to I atom speeds of 395 m s^{-1} at 304 nm and ~465 m s^{-1} at 282 nm. The two-color images [Figures 3(b) and 3(e)] are dominated by the exclusively probe-induced signal, but weak additional contributions are present at both larger and smaller radii. Under typical experimental conditions, the desired pump-induced two-color signal accounts for only ~15% of the total image intensity.

The magnitude of the one-color signal makes subtraction from the two-color signal challenging. The translational energy distributions derived from two-color and one-color images recorded back-to-back

13

were used to isolate the desired pump-induced distributions i.e. [pump + probe] – [probe only]. Unscaled

subtraction invariably led to bleaching at values of E_T that coincide with the λ_{probe}-dependent maxima in

the one-color distributions. This could be a consequence of CH_2I_2 parent depletion in the molecular beam

when the pump beam is present. The $P(E_T)$ arising from pump-induced dissociation should, however, be

independent of the choice of probe wavelength and can be recovered by minimizing the deviation

between the difference distributions measured at each independent probe wavelength by scaling the

probe-only contributions i.e. [pump + probe] – f[probe only], where f is a scaling factor. After deriving

the scaling factor, the scaled one-color images can be subtracted from the two-color images, as shown in

Figures 3(c) and 3(f). The procedure is illustrated in Figure 4 for detection of ground state I atoms at a

photolysis wavelength of 266 nm, for which we have independent measurements of the $P(E_T)$ from the

VUV ionization experiments. The agreement between the distributions obtained from the REMPI and

VUV data, shown in Figure 4(d), is excellent at $E_T < 1$ eV. The similarity of these distributions also

demonstrates that the VUV probe does not drive dissociative ionization of highly internally excited CH_2I

radicals to from $CH_2 + I^+$ to any significant extent. The small, fast and broad shoulder that appears

between ~1–2 eV in the REMPI difference distribution is absent in the VUV data but is attributed to a

small amount of multiphoton dissociation induced by the probe laser.

Translational energy distributions at each pump wavelength obtained from images probing I atoms are

presented in Figure 5. The distributions labelled "+MPI" are composites obtained from data acquired

using two different REMPI transitions, as described above. The conversion from speed to translational

energy assumed that CH_2I was the co-fragment. The $P(E_T)$ at pump wavelengths of 355 nm, 266 nm and

248 nm were obtained from two-color ion images recorded using VUV ionization, while those at 280 nm

and 304 nm were derived from one-color images using the REMPI probe scheme. Excitation at 355 nm

leads exclusively to ground state I + CH_2I, although I* atoms are also energetically accessible and results

in an E_T distribution that can be fit by a single Gaussian function centered at ~0.25 eV. The E_T

distribution cuts off well before the total available energy, $E_{AVL} = 1.34$ eV, at this excitation wavelength.

At the shorter pump wavelengths of 304 nm, 280 nm and 266 nm, the $P(E_T)$ can be broadly described by three components and are fit to an exponentially modified Gaussian function (EMG), which describes the slow statistical-like component that peaks near $E_T = 0$, and two Gaussian functions (G1 and G2), which represent the two faster components. The maximum observed E_T is < 1 eV at all pump wavelengths despite E_{AVL} ranging from 1.93–2.51 eV, indicating significant internal excitation of the CH_2I radical co-fragment. The slow component, which is first apparent at 304 nm, makes increasingly large contributions to the total $P(E_T)$ at shorter pump wavelengths. The G1 and G2 components are most distinct at 304 nm; G2 is reduced to a shoulder at 280 nm and 266 nm, and can no longer be resolved at 248 nm. The centers of G1 and G2 both move to higher E_T as E_{AVL} increases. The fraction of E_{AVL} partitioned into translational energy, $f_T = \langle E_T \rangle / E_{AVL}$, is 0.23±0.06 at 355 nm and decreases to only 0.15±0.02 at 248 nm.

Figure 6 shows translational energy distributions obtained probing I* atoms using 2+1 REMPI. The $P(E_T)$ at pump wavelengths of 266 nm and 248 nm are determined from two-color images using the scaled subtraction procedure described above. The scaled subtraction procedure results in excellent agreement between the $P(E_T)$ obtained from REMPI and VUV data for I atoms, shown in Figure 4, and provides confidence that it will also be reliable when probing I* atoms. The data at 304 nm and 282 nm are derived from one-color images. Qualitatively, the E_T distributions obtained probing I* shown in Figure 6 are similar to those shown in Figure 5. At all pump wavelengths, the E_T cutoff lies far below E_{AVL} and a slow component peaking near $E_T = 0$ makes an increasing contribution as the pump wavelength decreases. There is, however, only a single obvious faster component. The E_T distributions are again deconvolved by fitting to an exponentially modified Gaussian function to describe the slower component (EMG*) and a Gaussian function (G1*) to describe the faster component. At 304 nm, G1* is centered at 0.19 eV with FWHM of 0.10 eV. This feature shifts to greater E_T and broadens as E_{AVL} increases. At 248 nm, G1* is centered at $E_T = 0.35$ eV and has an equivalent FWHM. Similar fractions of the available energy are partitioned in to translational energy for I* atom products for which $f_T = 0.23±0.01$ at 304 nm, decreasing to 0.19±0.01 at 248 nm.

The peak centers obtained from the fits of the faster moving G1, G2 and G1* components shift to higher energy linearly with increasing excitation energy. Figure 7 shows the peak centers, E_{peak}, plotted against $(E_{pump} - E_{SO})$, the difference between the pump photon energy and the spin-orbit energy of the iodine atom. For spin-orbit excited I* atoms, $E_{SO} = 0.9426$ eV. The G1 and G1* components appear to fall on the same line and are distinct from G2. The C–I bond dissociation energy, D_0, can be determined from a linear fit to the data in Figure 7, assuming a linear increase in peak positions with increasing E_{AVL} beyond D_0. From the fit to the larger, combined G1+G1* data set, we obtain $D_0 = 2.155\pm0.008$ eV, where the quoted uncertainty represents the uncertainty in the fit. This result is in excellent agreement with $\Delta H = 2.24\pm0.06$ eV determined from thermochemical data at 298 K. A linear fit to the more limited G2 data returns a value of D_0 that is in agreement, although with significantly greater uncertainty ($D_0 = 2.17\pm0.18$ eV). Bailleux et al.[51] have inferred spin-orbit coupling constant of 1400 cm^{-1} (0.17 eV) for CH$_2$I. The common intercept suggests either that no spin-orbit excited CH$_2$I is formed in the dissociation or that the spin-orbit splitting is significantly smaller.

Speed-dependent, and ultimately E_T-dependent, anisotropy parameters, $\beta(E_T)$, were determined by radially integrating the sliced ion images and fitting the angular distributions to the usual expression

$$I(\theta) \propto 1 + \beta P_2(\cos\theta) \qquad (6)$$

where P_2 is the second Legendre polynomial and θ is the polar angle. In general, the observed values of β are positive at all E_T for all pump wavelengths and tends to increase from near zero, indicating a near-isotropic distribution, at low E_T. Inclusion of higher order Legendre polynomials did not improve the fit. For each pump wavelength, the variation of the anisotropy parameter with the translational energy is represented in Figure 8. The shaded area represents the uncertainty in β arising from fitting to equation (6) and repeated measurements. At longer pump wavelengths, the faster moving fragments dominate the distribution and are characterized by $\beta > 0$. At shorter wavelengths the slower component increases in importance, and the anisotropy is reduced. While the individual components are heavily overlapped at all pump wavelengths, it seems unlikely that there is any significant variation. At 304 nm, where the G1 and

16

G2 components are most readily distinguished, the values of β are effectively the same. E_T-averaged values of the anisotropy parameter, $\langle\beta\rangle$, are reported in Table 1. $\langle\beta\rangle$ varies somewhat with pump wavelength, being most anisotropic at 266 nm and decreasing slightly at both longer and shorter pump wavelengths, largely due to the increasing contribution of the near-isotropic EMG component. Spin-orbit excited I* atoms show slightly more anisotropic angular distributions than ground state I atoms, but the wavelength-dependent trends are the same.

The absorption spectrum calculated from spin-orbit MRCI calculations at the quadruple-zeta level is compared to experiment in Figure 9, with the calculated data shifted red by 27 nm and each transition broadened by 30 nm FWHM Gaussian. It can be seen that this leads to excellent agreement with experiment, especially in the region 265–360 nm. At shorter wavelengths, the weaker feature at ~250 nm is not reproduced by the calculations and the intensity of the band at 214 nm is overestimated, suggesting that larger active spaces and the inclusion of Rydberg states may be necessary for quantitatively correct results in this region, but such calculations are computationally intractable on currently available resources. Figure 9 also shows the major contributing peaks to the spectrum and it is evident that the long wavelength band is generally dominated by B_1 states. The weak shoulder near the long-wavelength onset of this band can be assigned to a B_2 state at roughly 355 nm. All of the excited states possess significant triplet character, which is presented as contributions to the spin-orbit eigenvectors in Table 2 along with vertical excitation energies and transition dipole moments.

The spin-orbit coupled potential energy curves (double-zeta level) calculated for the stretching of the C–I bond are shown in Figure 10. For clarity, only the first 16 spin-orbit states (out of the 33 resulting from the 17 spin-free electronic states) are shown, with all excluded higher energy states leading to higher energy dissociation products than those depicted. Technical difficulties meant that MOLPRO reverted to C_1 symmetry in many of the spin-orbit coupling calculations, yet assignment of states to A′ or A″ was straightforward from inspection of transition dipole moments. Calculations at the equilibrium geometry allowed each curve to be also assigned in C_{2v}-like symmetry, which is shown in the Figure legend, and

the eight excited states with the greatest oscillator strengths at the equilibrium geometry are emboldened. The electronically excited states shown in Figure 10 can be divided into four distinct groups (see Table 2), each similar in nature and leading to a different set of asymptotic products. Group I and II states are essentially repulsive and correlate with the first two product asymptotes, $CH_2I + I$ and $CH_2I + I^*$. The energy gap between group I and II states is ~0.84 eV at 4.2 Å, which is in excellent agreement with the energy difference between the ground $^2P_{3/2}$ and spin-orbit excited $^2P_{1/2}$ levels of iodine at this level of theory (0.86 eV). This is in agreement with the CASPT2 study of Liu et al.[18] The group III and IV states, which make increasingly important contributions to the absorption spectrum at shorter excitation wavelengths, are bound and correlate asymptotically with the formation of electronically excited $CH_2I + $ I/I*. Excited radical products are inaccessible at the excitation energies used in the current experiments; we note that the product asymptotes of the PECs show no splitting arising from spin-orbit coupling in the CH_2I radical.

Discussion

The translational energy distributions and anisotropy parameters measured in this work are in excellent agreement with previous one-color time-of-flight measurements by Jung et al. probing both I and I* at 304 nm. The ion imaging results of Xu et al.[22] agree at best qualitatively with the results of this work. Xu et al. derive values of $\beta > 1$ and show E_T distributions that are essentially invariant across the 277–304 nm range of excitation wavelengths. The tabulated peak positions derived from the decomposition of the E_T distributions disagree with the figures, suggesting an error in the presentation. In contrast, we find that $\langle \beta \rangle < 1$ generally. At pump wavelengths where the data are most directly comparable, our measurements indicate G1* components that are centered at $E_T = 0.19$ eV and 0.26 eV at at 304 nm and 282 nm, respectively, while Xu et al. report 0.24 eV and 0.25 eV. An analogous slow component that increased in magnitude at shorter pump wavelengths was also observed by Xu et al., although it remained a minor component.

18

Lehman *et al.* used VMI to study the photodissociation of CH_2I_2 at 248 nm, but probed only I* using a REMPI probe transition near 313 nm, which also generated strong one-color signals.[23] The E_T distribution derived from difference images appeared bimodal, and showed a pronounced dip at $E_T \approx 0.15$ eV (coinciding with the peak of the one-color E_T distributions) that is not present in the current measurements. While we agree that the translational energy distribution at a pump wavelength of 248 nm is bimodal, the dip in the earlier measurement of Lehman *et al.* may be an artifact of over-subtraction of the one-color signal. The anisotropy parameter of $\beta = 0.81 \pm 0.05$, however, is in reasonable agreement with our E_T-averaged value of $\langle \beta \rangle = 0.74 \pm 0.03$ at the same pump wavelength.

The results of our measurements support the consensus view that dissociation of CH_2I_2 after excitation in the near UV is prompt and that the bulk of the excess energy is partitioned into internal excitation of CH_2I. The translational energy distributions generally contain two distinct features – a slow component peaking near zero translational energy that increases in relative intensity at shorter wavelengths and faster non-zero peaking component(s). The slow component has been observed in previous imaging studies. We discount the possibility of three-body fragmentation to $CH_2 + I + I$ or unimolecular dissociation of internally excited CH_2I as the origin of the slow component on the basis of thermochemical data, which suggests a threshold wavelength of $\lambda_{pump} < 245$ nm. Furthermore, secondary dissociation of CH_2I photofragments by absorption of an additional photon is expected to lead to products with significant translational energy.[20] We have considered the effects of slicing on slow fragments, and tests using polar onion-peeling[52] to analyze unsliced images return near-identical speed distributions. The degree of translational energy release can be rationalized by the application of a simple impulsive model. In the "pure impulsive" model of Busch and Wilson,[53] the fraction of E_{AVL} partitioned into translation depends upon the ratio of the reduced masses of the atoms between which the bond breaks, μ_b, and the final photofragments, μ_f.

$$f_T = \mu_b / \mu_f \qquad (7)$$

The model assumes an instantaneous repulsion between the departing I atom and the CH_2 moiety, which is treated as a pseudo-atom, while the I atom that remains bound to C is initially a spectator. The model predicts $f_T = 0.19$, which is in reasonably good agreement with the 0.15–0.24 range observed experimentally. The wavelength-dependence of the translational energy release, however, cannot be accounted for using this model. The fractions of the available energy partitioned in to CH_2I vibration and rotation also depend on the kinematics, attenuated by the bond angle:

$$f_V = (1 - \mu_b/\mu_f) \cos^2 \alpha_0 \tag{8}$$

$$f_R = (1 - \mu_b/\mu_f) \sin^2 \alpha_0 \tag{9}$$

Using the experimental bond angle determined from microwave spectroscopy, $\alpha_0 = \angle(ICI) = 114.0°$,[54] the pure impulsive model predicts $f_V = 0.13$ and $f_R = 0.68$. The partitioning between vibrational and rotational excitation of the CH_2I fragments is not determined at the resolution obtainable in the VMI experiments. IR emission measurements after excitation at 248 nm and 308 nm by Baughcum and Leone indicate very high levels of vibrational excitation. Prominent features were observed in spectral regions corresponding to the C–H stretch ($\sim$3000 cm^{-1}), the CH_2 bend ($\sim$1300 cm^{-1}) and combinations of these two modes.[7] Emission in the region of the C–I stretch ($\sim$600 cm^{-1}) was also observed and resonance Raman studies have established that bond fission occurs following initial symmetric stretching of both C–I bonds.[17,55] Although not explicitly identified, it seems likely that the low frequency out-of-plane bend ($\sim$375 cm^{-1}) would also be excited as a result of the pyramidal-to-planar geometry change about the C atom following dissociation. The high degree of vibrational excitation observed in earlier experiments suggests that the impulsive model likely overstates the fraction of available energy partitioned into rotation of the CH_2I fragment.

At all excitation wavelengths, the photofragment angular distributions are anisotropic. In general, the anisotropy parameters derived from the images have values of $\beta > 0$, and generally increase steadily with increasing translational energy release. The limiting anisotropy parameter for a prompt dissociation is given by

$$\beta = 2P_2(\cos\chi) \tag{10}$$

where χ is the angle between the transition dipole moment of the parent molecule and the recoil velocity vector ($\boldsymbol{\mu} \cdot \boldsymbol{v}$). CH_2I_2 has C_{2v} symmetry, and transitions to states of A_1, B_1 and B_2 symmetry (with transition dipole moments oriented along the z, x, and y-axes, respectively) are electric dipole allowed. Following Demyanenko et al.,[56] axial recoil is defined as motion along the Jacobi coordinate $\boldsymbol{R}$, the vector between the departing I atom and the center of mass of the CH_2I radical, rather than along the C–I bond axis, which has been adopted by some authors.[22,23] The angle δ defines the orientation of the transition dipole moment to this vector ($\boldsymbol{\mu} \cdot \boldsymbol{R}$). Within the axial recoil limit, $\delta = \chi$ and the anisotropy parameters can be readily predicted using the geometry of CH_2I_2 determined from microwave spectroscopy.[54] For transition dipole moments corresponding to excitation to B_1, B_2 and A_1 states δ takes values of 3.6°, 90.0° and 86.4°, respectively and the limiting anisotropy parameters are predicted to be +1.99, –1 and –0.99. Only transitions to states of B_1 symmetry can result in $\beta > 0$.

The observation of photofragment anisotropy is indicative of prompt dissociation on a timescale less than the rotational period of the parent molecule. Slower dissociation could lead to the "statistical", isotropic components observed in the E_T distributions where $\beta(E_T) \approx 0$ after excitation at shorter wavelengths. For the faster moving components, $\beta > 0$ is consistent with dissociation on a repulsive surface of B_1 symmetry, although the anisotropy is significantly smaller than predicted for axial recoil following excitation to a pure B_1 state. One possible explanation is simultaneous excitation to states of A_1 or B_2 symmetry, both of which are predicted to result in $\beta \approx -1$, and would reduce the observed value of β. The difficulty of isolating individual components in the E_T distributions would suggest that the topology of the repulsive A_1 or B_2 surfaces contributing to the dissociation be similar to the B_1 state and lead to similar energy partitioning. This interpretation is broadly and qualitatively consistent with the results of the *ab initio* calculations. The calculated absorption spectrum is indeed dominated by transitions to states of B_1 symmetry (see Figure 9), accompanied by far weaker transitions to a few states of A_1 and B_2 symmetry. The contribution to the absorption cross section of the lowest energy 1 B_2 (1 A″) excited state

is very small and absorption is dominated by the 1 B_1 (3 A′) and 2 B_1 (4 A′) states at the longest excitation

wavelengths. All three of these states are repulsive and lead directly to CH_2I + I products. At shorter

wavelengths, the absorption is dominated by transitions to higher lying *bound states* of B_1 symmetry,

specifically the 3 B_1 (7 A′) and 4 B_1 (8 A′), with a smaller contribution from the bound 3 B_2 (8 A″) state.

Absorption to bound states at shorter wavelengths could be responsible for the near-isotropic slow

component in the $P(E_T)$ distributions, indicating some degree of trapping on the excited surface. The

bound states are crossed by repulsive states that correlate to I* products. None of the states correlating

with CH_2I + I* products is strongly absorbing; the most significant is the 3 A_1 (5 A′) state, which has a

transition dipole moment an order of magnitude smaller than the 1 B_1 and 2 B_1 states that dominate the

long-wavelength absorption. However, the generally larger values of $\langle \beta \rangle$ observed when probing I*

suggest that direct excitation to the 3 A_1 (5 A′) state does not make a major contributor to the dissociation

dynamics. The *ab initio* results imply that essentially all I* is produced via non-adiabatic transitions to

one of the four repulsive surfaces that correlate to the spin-orbit excited product asymptote.

The overall reduction and the general increase in β with increasing fragment translational energy may

additionally be a consequence of transverse recoil. Following the simple classical model of Demyanenko

et al.,[56] the deflection angle α between the recoil velocity $\boldsymbol{v}$ and the Jacobi coordinate $\boldsymbol{R}_c$ at some critical

distance at which the fragment angular momenta are established can be calculated using conservation of

energy and angular momentum:

$$\sin \alpha = \sqrt{I_{CH_2I} f_R / I_c f_T} \qquad (11)$$

Here I_{CH_2I} is the moment of inertia of the CH_2I fragment, approximated as a pseudo-diatomic classical

rotor, and I_c is the moment of inertia of the total system, evaluated at the distance R_c. In addition to the

critical distance, rotation of the Jacobi coordinate in the laboratory frame can be accounted for by

inclusion of a critical angle, α_c. Together, R_c and α_c define a geometry at which the final angular

momenta of the separating fragments are determined. In general they are not known *a priori*, but can be

used as fitting parameters. The variables f_R and f_T are the fractions of $(E_{AVL} - E_V)$ partitioned into rotation

and translation, respectively. The anisotropy parameter can be calculated using equation (10) where $\chi = \alpha_c + \alpha$. Transverse recoil, characterized by large values of α, will be important when f_R is large relative to f_T and the moment of inertia of the system at the critical distance and angle is comparable to that of the nascent CH_2I radical fragment. As a limiting case we assume impulsive dissociation, that is, the angular momenta are established immediately and the critical distance and angle are determined by the parent molecule geometry. In this case, $R_c = 3.4$ Å and $\alpha_c = \delta = 3.6$ for a transition to a B_1 state. Using the energy partitioning predicted by the impulsive model ($f_R = 0.68$, $f_T=0.19$) results in a deflection angle of $\alpha = 31.1°$ and an anisotropy parameter of $\beta = 1.03$, which is in reasonably good agreement with the experimental results. Increasing the fraction of the available energy partitioned into vibration (or equivalently, reducing f_R while holding f_T constant) causes β to increase. With $f_V = 0.26$ and $f_R = 0.55$, the predicted anisotropy parameter is $\beta = 1.19$. While a more quantitative approach using R_c and α_c as fitting parameters to model the E_T-dependent anisotropy parameter, is in principle possible, it is unfeasible because the vibrational population distribution is unknown.

The photochemistry of CH_2I_2 can be compared to that of other iodine-containing molecules. CH_3I has been extensively studied and its photochemistry has been recently been summarized by Gardiner et al.[50] The first absorption band results from excitation to states labelled $^1Q_1$, $^3Q_0$ and $^3Q_1$ that are dissociative along the C–I coordinate. Parallel transition to the $^3Q_0$ state is predominantly responsible for the absorption spectrum and correlates with CH_3 + I*, although the photochemistry is complicated by the existence of a conical intersection with the $^1Q_1$ state. In general, the excess energy is partitioned almost entirely into relative translation and a strong preference for production of spin-orbit excited I* atoms is observed, in marked contrast to CH_2I_2. Larger fractions of the available energy are partitioned into the alkyl radical fragments following photodissociation of larger alkyl iodides, although the propensity for production of I* over I remains and the analogous electronic states determine the photochemistry.[50,57] The long-wavelength photochemistry of CH_2BrI is perhaps more directly comparable to CH_2I_2.[58] At 248 nm, dissociation to form CHBr + I dominates and the behavior is generally similar to CH_2I_2; specifically,

23

the transitions are predominantly parallel in character, the majority of the available energy is partitioned into the radical fragment, and the I/I* spin-orbit branching also favors the ground state.

Finally, we consider the implications for kinetics studies which use photolysis of CH_2I_2 as a source of CH_2I radicals. CH_2I is formed in conjunction with both I and I* atoms at all but the longest pump wavelengths. The translational energy releases are in general similar and relatively small, resulting in E_{INT} distributions for CH_2I that depend primarily on the spin-orbit state formed. Overall E_{INT} distributions are constructed by weighting the distributions obtained probing either I or I* by the appropriate quantum yields.[8] The resulting distributions are shown in Figure 11 for λ_{pump} = 355 nm, 266 nm, and 248 nm, corresponding to laser wavelengths (Nd:YAG 3rd and 4th harmonic or KrF excimer) that are commonly used to prepare CH_2I radicals for kinetics studies. At 355 nm, CH_2I radicals are formed only in conjunction with ground state I atoms resulting in a unimodal internal energy distribution with $\langle E_{INT}\rangle$ = 1.03±0.08 eV. At shorter wavelengths, the E_{INT} distributions for the CH_2I radicals extend to even higher energy and contain two distinct components corresponding to formation of I and I* atoms. For example, at 248 nm, where the branching to I and I* is similar, an approximately equal amount of CH_2I radicals will be formed with $\langle E_{INT}\rangle$ = 2.42±0.02 eV in conjunction with I atoms, and $\langle E_{INT}\rangle$ = 1.55±0.02 eV for those formed with I*.

Recently, we have investigated the kinetics of the reaction between CH_2I and O_2 using cavity ring-down spectroscopy to probe IO radical products, using 355 nm photolysis of CH_2I_2 to generate iodomethyl radicals.[13] IO radicals were found to be produced in both $v = 0$ and $v = 1$, the latter with a significantly larger bimolecular rate constant, but a far smaller yield. It was proposed that the photolytically-generated hot CH_2I* radicals react with O_2 to form $IO(v = 0,1)$ directly and promptly prior to thermalization, while the majority of $IO(v = 0)$ production occurs more slowly via the $CH_2OO + I$ reaction. Photolysis of CH_2I_2 at 266 nm and 248 nm produces CH_2I radicals with even greater internal excitation. Caution is necessary in the interpretation of kinetics studies that use photolysis as a means to generate reactive radicals for

kinetics studies, particularly if performed at low pressures where the assumption of thermalization prior to reaction may not be valid.

Conclusions

The photodissociation dynamics of CH_2I_2 following excitation over a range of wavelengths has been examined experimentally using velocity-map ion imaging, using both state-selective REMPI and single-photon VUV ionization to detect I and I* products. The images show only modest translational energy release, indicating significant partitioning of the available energy into the internal modes of the CH_2I radical co-fragment. Analysis of the photofragment anisotropy results in weakly speed-dependent positive anisotropy parameters, suggesting excitation to B_1 states. The reduction from the limiting value of +2 is attributed to both weak contributions to the absorption from states of A_1 and B_2 symmetry and transverse recoil. The experimental observations are supported by complementary high-level *ab initio* calculations that have mapped out the spin-orbit coupled electronically excited states responsible for the first absorption bands. The calculations indicate that the absorption spectrum is dominated by transitions to states of B_1 symmetry and all states have significant triplet character; the lower energy states accessed at longer wavelengths are purely repulsive, but excitation at shorter wavelengths accesses bound states that dissociate by rapid non-adiabatic coupling to nearby repulsive surfaces.

Acknowledgements

References

1 L. J. Carpenter, *Chem. Rev.*, 2003, **103**, 4953–4962.

2 A. Saiz-Lopez, J. M. C. Plane, A. R. Baker, L. J. Carpenter, R. von Glasow, J. C. Gómez Martín, G. McFiggans and R. W. Saunders, *Chem. Rev.*, 2012, **112**, 1773–1804.

3 W. L. Chameides and D. D. Davis, *J. Geophys. Res.*, 1980, **85**, 7383–7398.

4 K. A. Read, A. S. Mahajan, L. J. Carpenter, M. J. Evans, B. V. E. Faria, D. E. Heard, J. R. Hopkins, J. D. Lee, S. J. Moller, A. C. Lewis, L. Mendes, J. B. McQuaid, H. Oetjen, A. Saiz-Lopez, M. J. Pilling and J. M. C. Plane, *Nature*, 2008, **453**, 1232–1235.

5 C. M. Roehl, J. B. Burkholder, G. K. Moortgat, A. R. Ravishankara and P. J. Crutzen, *J. Geophys. Res.*, 1997, **102**, 12819–12829.

6 J. C. Mössinger, D. E. Shallcross and R. A. Cox, *J. Chem. Soc., Faraday Trans.*, 1998, **94**, 1391–1396.

7 S. L. Baughcum and S. R. Leone, *J. Chem. Phys.*, 1980, **72**, 6531–6545.

8 J. B. Koffend and S. R. Leone, *Chem. Phys. Lett.*, 1981, **81**, 136–141.

9 T. F. Hunter and K. S. Kristjansson, *Chem. Phys. Lett.*, 1982, **90**, 35–40.

10 S.-Y. Chen, P.-Y. Tsai, H.-C. Lin, C.-C. Wu, K.-C. Lin, B. J. Sun and A. H. H. Chang, *J. Chem. Phys.*, 2011, **134**, 034315.

11 C. A. Taatjes, D. E. Shallcross and C. J. Percival, *Phys. Chem. Chem. Phys.*, 2014, **16**, 1704–1718.

12 D. L. Osborn and C. A. Taatjes, *Int. Rev. Phys. Chem.*, 2015, **34**, 309–360.

13 E. S. Foreman and C. Murray, *J. Phys. Chem. A*, 2015, **119**, 8981–8990.

14 M. Ito, P. C. Huang and E. M. Kosower, *Trans. Faraday Soc.*, 1961, **57**, 1662–1673.

15 M. Kawasaki, S. J. Lee and R. Bersohn, *J. Chem. Phys.*, 1975, **63**, 809–814.

16 A. Gedanken and M. D. Rowe, *Chem. Phys.*, 1979, **36**, 181–186.

17 X. Zheng and D. L. Phillips, *Chem. Phys. Lett.*, 2000, **316**, 524–530.

18 Y.-J. Liu, L. De Vico, R. Lindh and W.-H. Fang, *ChemPhysChem*, 2007, **8**, 890–898.

19 A. Mandal, P. J. Singh, A. Shastri and B. N. Jagatap, *J. Chem. Phys.*, 2014, **140**, 194312.

20 P. M. Kroger, P. C. Demou and S. J. Riley, *J. Chem. Phys.*, 1976, **65**, 1823–1834.

21 K.-W. Jung, T. S. Ahmadi and M. A. El-Sayed, *B. Korean Chem. Soc.*, 1997, **18**, 1274–1280.

22 H. Xu, Y. Guo, S. Liu, X. Ma, D. Dai and G. Sha, *J. Chem. Phys.*, 2002, **117**, 5722–5729.

23 J. H. Lehman, H. Li and M. I. Lester, *Chem. Phys. Lett.*, 2013, **590**, 16–21.

24 D. Townsend, M. P. Minitti and A. G. Suits, *Rev. Sci. Instrum.*, 2003, **74**, 2530–2539.

25 R. A. Livingstone, J. O. F. Thompson, M. Iljina, R. J. Donaldson, B. J. Sussman, M. J. Paterson and D. Townsend, *J. Chem. Phys.*, 2012, **137**, 184304.

26 M. L. Lipciuc and M. H. M. Janssen, *Phys. Chem. Chem. Phys.*, 2006, **8**, 3007–3016.

27 G. Guelachvili, D. de Villeneuve, R. Farrenq, W. Urban and J. Verges, *J. Mol. Spectrosc.*, 1983, **98**, 64–79.

28 T. Suzuki, H. Katayanagi, S. Nanbu and M. Aoyagi, *J. Chem. Phys.*, 1998, **109**, 5778–5794.

29 M. Brouard, A. V. Green, F. Quadrini and C. Vallance, *J. Chem. Phys.*, 2007, **127**, 084304.

30 M. L. Lipciuc, T. P. Rakitzis, W. L. Meerts, G. C. Groenenboom and M. H. M. Janssen, *Phys. Chem. Chem. Phys.*, 2011, **13**, 8549–8559.

31 T. B. Adler, G. Knizia and H.-J. Werner, *J. Chem. Phys.*, 2007, **127**, 221106.

32 G. Knizia, T. B. Adler and H.-J. Werner, *J. Chem. Phys.*, 2009, **130**, 054104.

33 K. A. Peterson, T. B. Adler and H.-J. Werner, *J. Chem. Phys.*, 2008, **128**, 084102.

34 J. G. Hill and K. A. Peterson, *J. Chem. Phys.*, 2014, **141**, 094106.

35 K. A. Peterson, D. Figgen, E. Goll, H. Stoll and M. Dolg, *J. Chem. Phys.*, 2003, **119**, 11113–11123.

36 F. Weigend, *Phys. Chem. Chem. Phys.*, 2002, **4**, 4285–4291.

37 F. Weigend, *J. Comput. Chem.*, 2008, **29**, 167–175.

38 C. Hättig, *Phys. Chem. Chem. Phys.*, 2005, **7**, 59–66.

39 E. F. Valeev, *Chemical Physics Letters*, 2004, **395**, 190–195.

40 K. E. Yousaf and K. A. Peterson, *J. Chem. Phys.*, 2008, **129**, 184108.

41 T. Shiozaki, G. Knizia and H.-J. Werner, *J. Chem. Phys.*, 2011, **134**, 034113.

42 T. Shiozaki and H.-J. Werner, *J. Chem. Phys.*, 2011, **134**, 184104.

43 E. R. Davidson and D. W. Silver, *Chemical Physics Letters*, 1977, **52**, 403–406.

44 T. Shiozaki and H.-J. Werner, *J. Chem. Phys.*, 2010, **133**, 141103.

45 K. A. Peterson, C. Krause, H. Stoll, J. G. Hill and H.-J. Werner, *Mol. Phys.*, 2011, **109**, 2607–2623.

46 T. H. Dunning Jr., *J. Chem. Phys.*, 1989, **90**, 1007–1023.

47 H.-J. Werner, P. J. Knowles, G. Knizia, F. R. Manby and M. Schütz, *Comput. Mol. Sci.*, 2012, **2**, 242–253.

48 *MOLPRO, version 2012.1, a package of ab initio programs, H.-J. Werner, P. J. Knowles, G. Knizia, F. R. Manby, M. Schütz, P. Celani, T. Korona, R. Lindh, A. Mitrushenkov, G. Rauhut, K. R. Shamasundar, T. B. Adler, R. D. Amos, A. Bernhardsson, A. Berning, D. L. Cooper, M. J. O. Deegan, A. J. Dobbyn, F. Eckert, E. Goll, C. Hampel, A. Hesselmann, G. Hetzer, T. Hrenar, G. Jansen, C. Köppl, Y. Liu, A. W. Lloyd, R. A. Mata, A. J. May, S. J. McNicholas, W. Meyer, M. E. Mura, A. Nicklass, D. P. O'Neill, P. Palmieri, D. Peng, K. Pflüger, R. Pitzer, M. Reiher, T. Shiozaki, H. Stoll, A. J. Stone, R. Tarroni, T. Thorsteinsson, and M. Wang, , see http://www.molpro.net., .*

49 H. Fan and S. T. Pratt, *J. Phys. Chem. A*, 2007, **111**, 3901–3906.

50 S. H. Gardiner, M. L. Lipciuc, T. N. V. Karsili, M. N. R. Ashfold and C. Vallance, *Phys. Chem. Chem. Phys.*, 2015, **17**, 4096–4106.

51 S. Bailleux, P. Kania, J. Skřínský, T. Okabayashi, M. Tanimoto, S. Matsumoto and H. Ozeki, *J. Phys. Chem. A*, 2010, **114**, 4776–4784.

52 G. M. Roberts, J. L. Nixon, J. Lecointre, E. Wrede and J. R. R. Verlet, *Rev. Sci. Instrum.*, 2009, **80**, 053104–7.

53 G. E. Busch and K. R. Wilson, *J. Chem. Phys.*, 1972, **56**, 3626.

54 Z. Kisiel, L. Pszczółkowski, W. Caminati and P. G. Favero, *J. Chem. Phys.*, 1996, **105**, 1778–1785.

55 W. M. Kwok and D. L. Phillips, *Chem. Phys. Lett.*, 1997, **270**, 506–516.

56 A. V. Demyanenko, V. Dribinski, H. Reisler, H. Meyer and C. X. W. Qian, *J. Chem. Phys.*, 1999, **111**, 7383–7396.

57 Y. Liu, Q. Zheng, Y. Zhang, R. Zhang, Y. Wang and B. Zhang, *ChemPhysChem*, 2009, **10**, 830–834.

58 L. J. Butler, E. J. Hintsa, S. F. Shane and Y. T. Lee, *J. Chem. Phys.*, 1987, **86**, 2051–2074.

Tables

Table 1. Total available energy E_{AVL}, average translational energy $\langle E_T \rangle$, average CH_2I internal energy $\langle E_{INT} \rangle$, and E_T-averaged anisotropy parameters $\langle \beta \rangle$ obtained from analysis of ion images of I and I* atoms arising from CH_2I_2 photodissociation at several pump wavelengths.

	I				I*			
λ_{pump} / nm	E_{AVL} / eV	$\langle E_T \rangle$ / eV	$\langle E_{INT} \rangle$ / eV	$\langle \beta \rangle$	E_{AVL} / eV	$\langle E_T \rangle$ / eV	$\langle E_{INT} \rangle$ / eV	$\langle \beta \rangle$
248	2.844(11)	0.42(4)	2.42(4)	0.85(4)	1.902(5)	0.36(2)	1.55(2)	0.74(3)
266	2.506(10)	0.40(2)	2.10(2)	0.90(3)	1.563(4)	0.35(3)	1.21(3)	0.99(5)
280/282	2.278(9)	0.444(2)	1.83(1)	0.33(1)	1.304(4)	0.294(8)	1.01(1)	0.49(1)
304	1.927(7)	0.461(8)	1.47(1)	0.21(1)	0.981(3)	0.227(9)	0.75(1)	0.45(1)
355	1.338(5)	0.31(8)	1.03(8)	0.37(9)	0.395(1)	–	–	–

Table 2. Spin-orbit coupled (quadruple-zeta) vertical excitation energies ($E-E_1$), transition dipole moments (TDM) and major contributions to the spin-orbit eigenvectors at the equilibrium geometry.

State	Group	State number[a]	$E-E_1$ / eV	TDM / D	Major contributions (> 5%)		
X A$_1$ (X A′)		1	0.000		99% 1^1A_1		
1 B$_2$ (1 A″)	I	3	3.858	0.077	64% 1^3B_2	23% 1^3A_2	11% 2^1A_1
1 B$_1$ (3 A′)	I	5	4.136	0.346	82% 2^1A_1	10% 1^3B_2	
2 B$_1$ (4 A′)	I	7	4.207	0.643	69% 3^1A_1	14% 2^3B_2	9% 2^3A_2
3 A$_1$ (5 A′)	II	8	4.275	0.055	68% 3^3B_1	26% 2^3A_2	
2 B$_2$ (4 A″)	I	9	4.345	0.240	80% 2^3B_2	8% 3^1A_1	6% 2^3A_2
3 B$_1$ (7 A′)	III	12	4.617	0.641	48% 1^3A_2	35% 1^1B_1	17% 1^3A_1
4 B$_1$ (8 A′)	III	14	4.846	0.438	38% 1^3A_1	30% 1^1B_1	29% 1^3B_2
4 B$_2$ (8 A″)	III	16	4.990	0.374	62% 2^1B_1	37% 2^3A_2	
5 A$_1$ (9 A′)	IV	17	5.147	0.180	80% 2^3B_1	16% 3^3A_1	

[a] States 2, 10 and 11 (2 A$_1$, 3 B$_2$, and 4 A$_1$) have TDM < 0.05 D and are not listed. States 4, 6, 13, and 15 have A$_2$ symmetry.
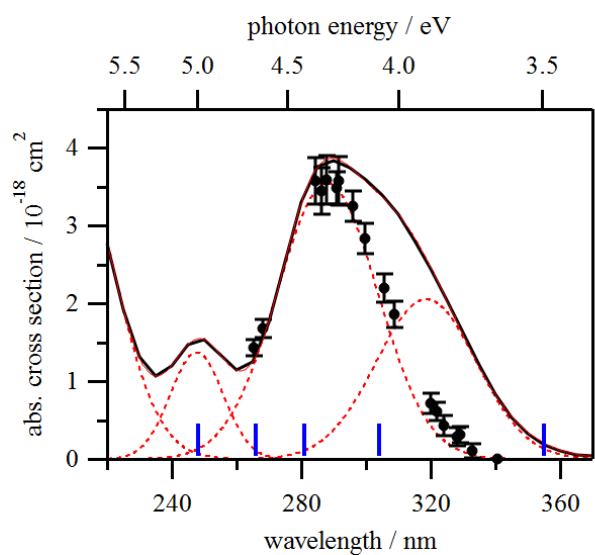
Figure 1. Absorption spectrum for CH_2I_2 (black) measured by Roehl *et al*., overlaid with individual Gaussian components (red). The black symbols indicate relative I* quantum yields weighted by the absorption cross section, as measured by Koffend and Leone. The vertical blue lines indicate the pump wavelengths used in this work.
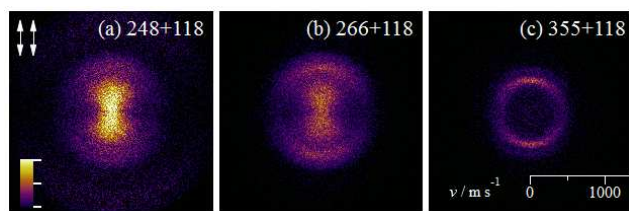
Figure 2. Ion images of I atom products of the photodissociation of CH_2I_2 for $\lambda_{pump} + \lambda_{probe}$ (in nm): (a) 248 + 118, (b) 266 + 118 and (c) 355 + 118. Small background pump-only and probe-only signals have been subtracted.
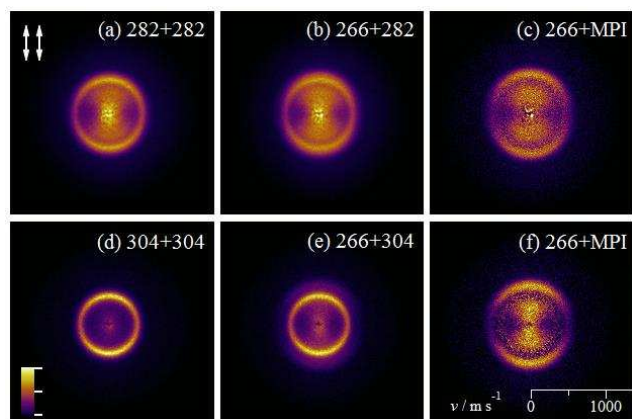
Figure 3. Ion images of I* products detected with REMPI after the photodissociation of CH_2I_2 at $\lambda_{pump} + \lambda_{probe}$ (in nm). Top row: (a) 282 + 282, (b) 266 + 282, (c) 266 + MPI difference image obtained from scaled subtraction i.e. (b) – f(a). Bottom row: (d) 304 + 304, (e) 266 + 304, (f) 266 + MPI difference image obtained from scaled subtraction i.e. (e) – f(d)
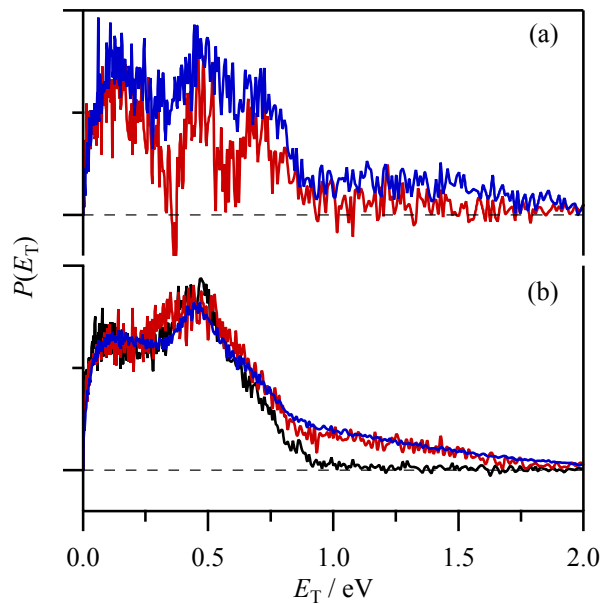
Figure 4. Illustration of subtraction procedure for REMPI measurements at a pump wavelength of 266 nm and probing ground state I atoms. (a) unscaled [pump+probe]–[probe] E_T distributions obtained probing at 280 nm (blue) and 304 nm (red). The dips occur where the one-color distributions have maxima. (b) E_T distributions after subtracting scaled one-color distributions as described in the text. The E_T distribution obtained independently using VUV ionization (black) is shown for comparison.
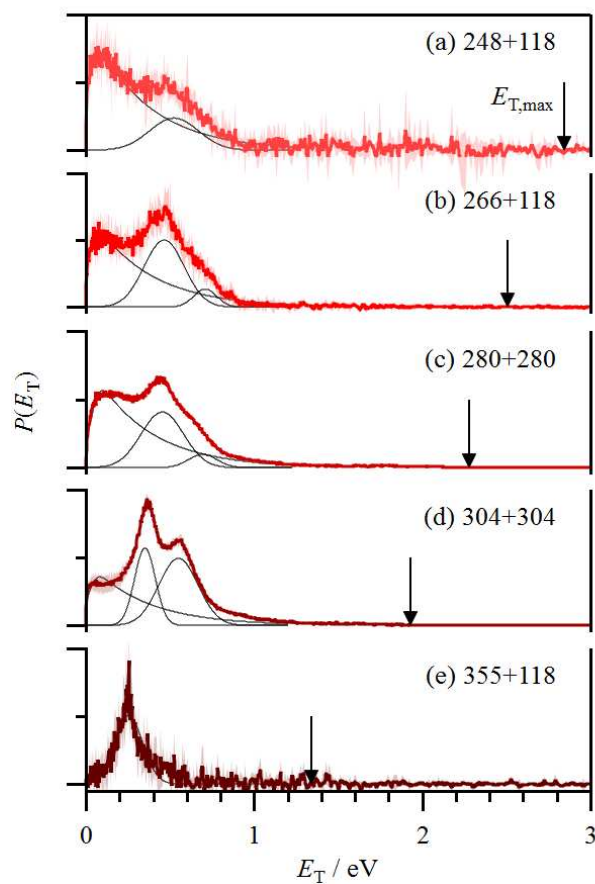
Figure 5. Translational energy distributions derived from I atom images following photodissociation of CH_2I_2 for combinations of $\lambda_{pump} + \lambda_{probe}$ (in nm). (a) 248 + 118, (b) 266 + 118, (c) 280 + 280, (d) 304 +304 and (e) 355 +118. All distributions are normalized to the same area and displayed on the same vertical scale. The thin black lines indicate components of the fits, which are described in the text.
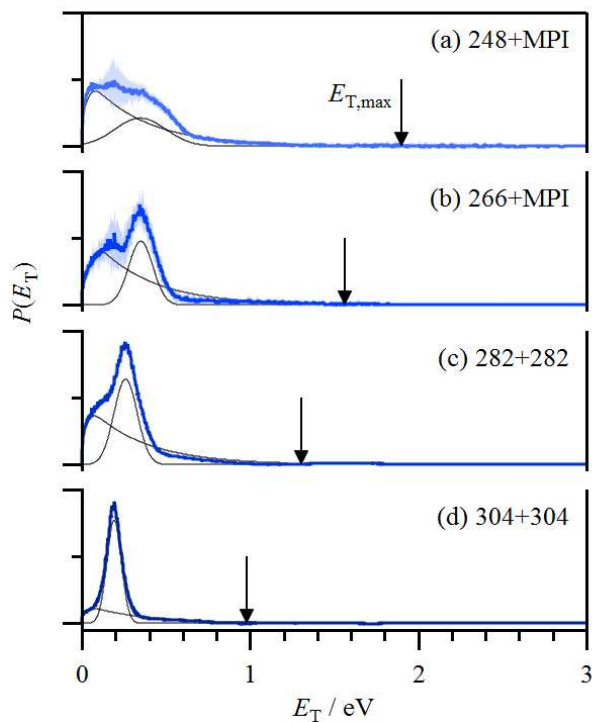
Figure 6. Translational energy distributions derived from I*
atom images following photodissociation of CH_2I_2 for
combinations of $\lambda_{pump} + \lambda_{probe}$ (in nm). (a) 248 + REMPI, (b)
266 + REMPI, (c) 280 + 280 and (d) 304 + 304. REMPI probe
refers to the average distribution obtained from two
independent probe transitions. All distributions are normalized
to the same area and displayed on the same vertical scale. The
thin black lines indicate components of the fits, which are
described in the text.
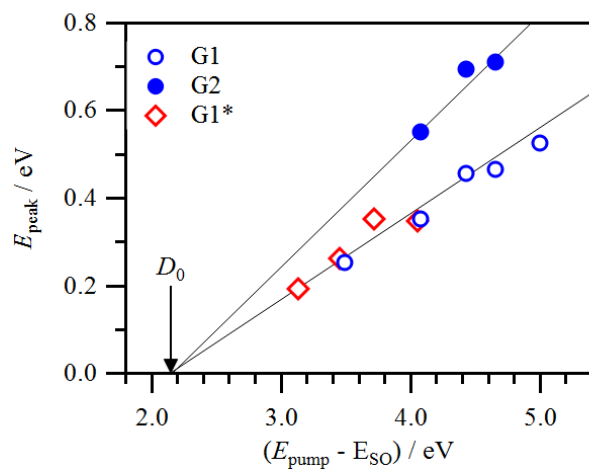
Figure 7. Peak centers of intermediate (G1/G1*) and fast (G2) Gaussian components of the E_T distributions plotted as a function of the difference between the pump photon energy and the spin-orbit energy of the probed I (blue) or I* (red) atom.
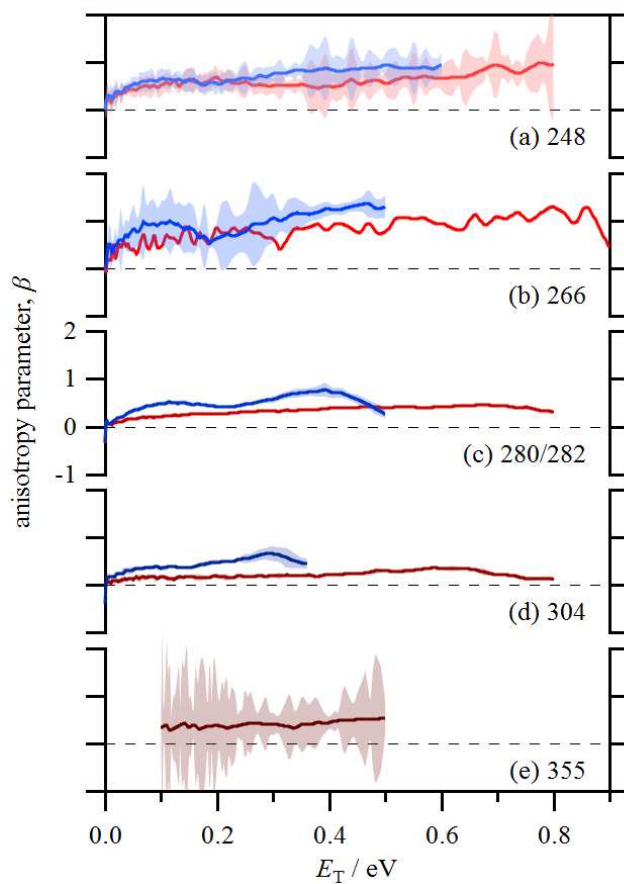
Figure 8. E_T-dependent anisotropy parameters derived from ion images probing I (red) and I* (blue) at the excitation wavelengths (a) 248 nm, (b) 266 nm, (c) 280/282 nm, (d) 304 nm, and (e) 355 nm.
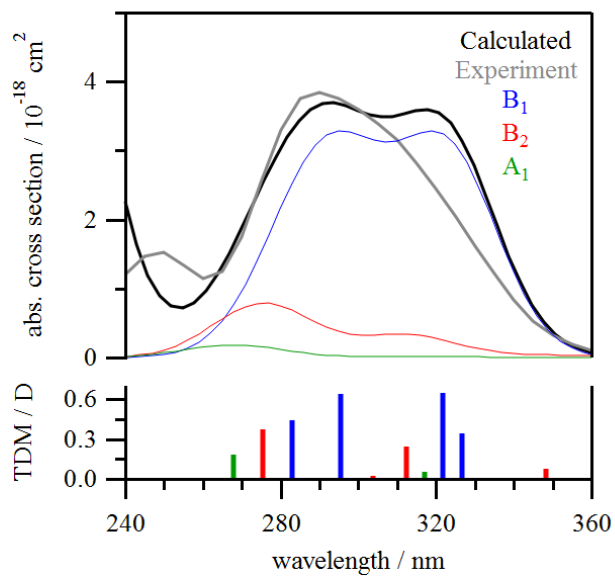
Figure 9. Upper panel: calculated absorption spectrum (shifted red by 27 nm) compared to experiment. Each vertical transition, shown in the lower panel, has been broadened by a 30 nm FWHM Gaussian function.
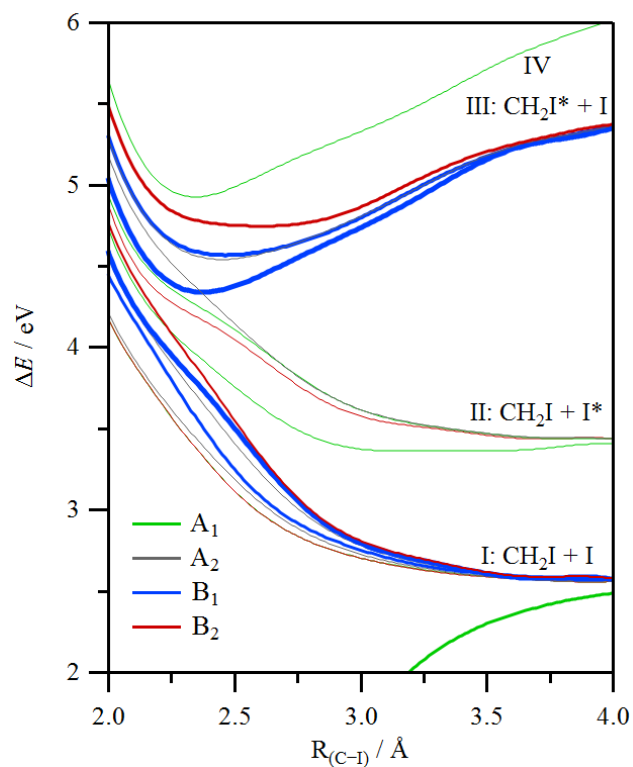
Figure 10. Potential energy curves with respect to the C–I bond coordinate including spin-orbit coupling. States corresponding to excitations with significant transition dipole moments have thicker lines and symbols.
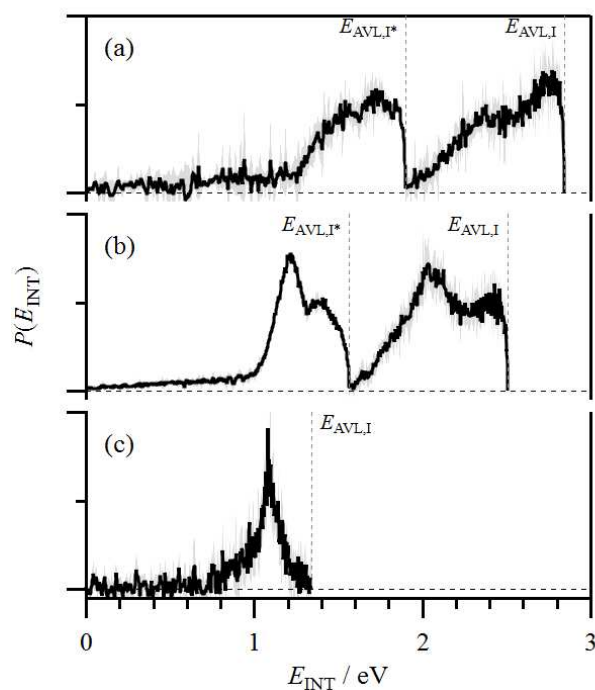
Figure 11. Overall CH$_2$I internal energy distributions, constructed from I and I* measurements weighted by respective quantum yields at pump wavelengths of (a) 248 nm, (b) 266 nm, and (c) 355 nm.